J. Fluid Mech. (2001), *vol.* 440, *pp.* 27–47. Printed in the United Kingdom

Feedback control of weakly nonlinear Rayleigh–Bénard–Marangoni convection

By A. C. OR AND R. E. KELLY

Department of Mechanical & Aerospace Engineering, University of California, Los Angeles, CA 90095-1597, USA

(Received 2 May 2000 and in revised form 4 October 2000)

We study the effect of proportional feedback control on the onset and development of finite-wavelength Rayleigh–Bénard–Marangoni (RBM) convection using weakly nonlinear theory as applied to Nield's model, which includes both thermocapillarity and buoyancy but ignores deformation of the free surface. A two-layer model configuration is used, which has a purely conducting gas layer on top of the liquid. In the feedback control analysis, a control action in the form of temperature or heat flux is considered. Both measurement and control action are assumed to be continuous in space and time. Besides demonstrating that stabilization of the basic state can be achieved on a linear basis, the results also indicate that a wide range of weakly nonlinear flow properties can also be altered by the linear and nonlinear control processes used here. These include changing the nature of hexagonal convection and the amount of subcritical hysteresis associated with subcritical bifurcation.

1. Introduction

We have recently demonstrated that the long-wavelength mode of Bénard–Marangoni (BM) convection (see VanHook *et al.* 1998), which tends to cause rupture of thin heated films bounded on one side by a gas, can be prevented by applying feedback control at the lower wall (Or *et al.* 1999). By means of a nonlinear control law, it was shown that a linear gain can increase the critical value of the Marangoni number and that a quadratic gain can eliminate the subcritical range of instability. In BM convection, the long-wavelength mode occurs prior to the finite wavelength (or Pearson) mode when the layer is sufficiently thin or when gravity is significantly reduced (such as in the case of Space experiments). If a thicker liquid layer is considered or gravity is increased, the Pearson mode will occur first provided that the layer is still thin enough for buoyancy to be negligible. Rayleigh–Bénard (RB) convection will occur eventually with non-zero gravity as the thickness of the layer increases. As a follow-up to our previous investigation, we focus here on the finite-wavelength mode driven by surface tension as well as by buoyancy, which we refer to as Rayleigh–Bénard–Marangoni (RBM) convection.

The onset problem of RBM convection for a non-deformable free surface without control was first investigated by Nield (1964) but Smith (1966) further showed that interfacial deformation exerts insignificant effects provided that the terrestrial value of gravity is typical and that the liquid layer is thick enough that the long-wavelength instability does not occur. We will use Nield's model, in which the interface is assumed to be non-deformable, and focus on the weakly nonlinear RB and BM problems. The BM problem, in particular, has been studied by a number

of authors for the uncontrolled situation (see Bestehorn 1993, 1994; Schatz *et al.* 1995; Parmentier *et al.* 1996; Bragard & Velarde 1998). In certain cases, a deformable interface was incorporated, such as by Golovin, Nepomnyashchy & Pismen (1995). Like the long-wavelength mode we studied earlier (Or *et al.* 1999), the Pearson mode is associated with a subcritical instability. But RB convection with a nondeformable free surface is not associated with a subcritical instability despite the asymmetric boundary conditions on the upper and lower surfaces. The absence of subcriticality in RB convection is apparent in Bestehorn's results (1994, see his figure 3; see also Clever & Busse 1993). In regard to experimental investigations, Schatz *et al.* (1995) have studied the onset of the Pearson mode for BM convection as well as the effects of subcritical hysteresis based on a gas–liquid layer configuration. More results concerning onset were presented by Schatz *et al.* (1999). Their results provide a basis for comparison of our theoretical results for the uncontrolled problem. Some discrepancies are discussed.

While a single-layer geometry with a free surface is advantageous for mathematical simplicity, recent laboratory experiments (see Koschmieder & Switzer 1992 and Schatz *et al.* 1995) have adopted a two-layer configuration in order to achieve well-defined thermal boundary conditions. In the experiments, a gas layer separates the liquid from the upper conducting wall. We consider here a purely conductive, massless and frictionless gas layer. Pérez-García, Echebarria & Bestehorn (1998) have employed this conductive-gas hypothesis which they referred to as the minimal two-layer model and have provided a linear analysis of the Pearson mode for general thermal boundary conditions. In recent work, Regnier, Dauby & Lebon (2000) have argued that motion in the gas layer can be ignored when the thickness of the gas layer is less than that of the liquid layer.

In the case of RB convection, linear feedback control was studied by Tang & Bau (1994, 1998*a*, *b*) and by Howle (1997*a*, *b*, *c*, 2000). Although different types of thermal boundary conditions as well as different types of sensors and actuators were used in the theoretical models, the theory predicts in both cases a significant increase in the stable range of the basic state. Although less stabilization was obtained in the initial experiments on small aspect ratio containers by Tang & Bau (1998*a*) and Howle (1997*b*), another experiment by Howle (1997*c*) with a moderate aspect ratio container indicated that substantial stabilization is indeed possible. Bau (1999) also studied theoretically the onset of the Pearson mode of BM convection on a linear basis, using a feedback control approach involving the wall temperature. An important result from these studies is the prediction of oscillatory instability at large values of gain, which limits the degree of stabilization achievable in the planar sensor models. After the onset of oscillations, the amount of stabilization declines as the gain increases and eventually destabilization occurs.

The amount of stabilization predicted from the linear analysis is valid only when the initial state is perturbed by infinitesimally small disturbances. If a finite-amplitude initial disturbance has to be damped out by the control, both nonlinear dynamics and nonlinear control action have to be considered if the uncontrolled system has subcritical instabilities, such as for BM convection. The weakly nonlinear control problem for RB convection was first considered by Shortis & Hall (1996) who used an expansion based on not only the Rayleigh number being close to the critical value so that the difference is small but also the control gain being of the same order, i.e. small. This assumption naturally restricts the validity of their results to values of the Rayleigh number close to the critical value existing without control. We remove this restriction by considering the non-dimensional gain to be $O(1)$. We also use boundary

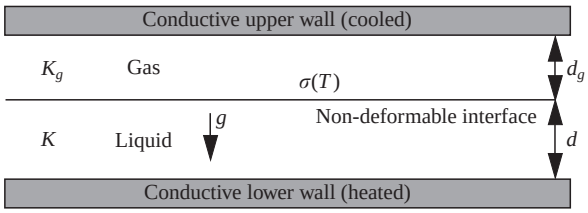

FIGURE 1. The geometric configuration (side view).

conditions that are more typical of an actual experiment than the stress-free conditions used by Shortis & Hall (1996). Their analysis is also problematic because the total temperature is used in the control law rather than only the disturbance temperature as done in the other analyses mentioned above. Nonetheless, the qualitative nature of the results of Shortis & Hall (1996) agrees with our own results in the RB limit.

We consider a weakly nonlinear analysis using Nield's model with a minimal two-layer modification. Both linear and nonlinear stability properties will be investigated for the uncontrolled and controlled situations. In addition to the imposed temperature boundary condition for the lower wall, we also consider the case of an imposed heat flux for both situations. In § 2, we shall formulate the mathematical problem which leads to cubic-order amplitude equations. We start § 3 with results on the uncontrolled system and comparisons with known theoretical and experimental results. Also, the theoretical results are extended to some parameter regimes which have not been investigated previously, such as the dependence of the subcritical hysteresis on the thickness ratio between the two fluids. We focus then on the effects of feedback control upon the instability of the basic state and the weakly nonlinear planforms. In § 4, we conclude the paper with some overall remarks.

2. Mathematical formulation

Consider an infinite horizontal layer of liquid of thickness d, bounded below by a rigid conductive wall (at $z^* = 0$) and above by a layer of gas of thickness d_g. The gas in turn is bounded from above by another rigid wall (at $z^* = d + d_g$). For the basic state, a constant temperature T_t^* is maintained at the upper wall but either a constant temperature T_b^* or an upward constant heat flux Q_0^* is imposed at the lower wall. The two-layer system is sketched in figure 1. Since the basic state is purely conductive, its temperature profile is piecewise linear. For the case of an imposed temperature at the lower wall, we write $T^*(z^*) = T_b^* + \Delta T_0^* T(z)$ where ΔT_0^* is the temperature difference over the liquid layer and $T(z)$ (with $z = z^*/d$) is the non-dimensional basic temperature. For the case of imposed heat flux at the lower wall, we write $\mathrm{d}T^*/\mathrm{d}z^* = (\Delta T_0^*/d)(\mathrm{d}T/\mathrm{d}z)$ instead. For convenience, the two cases of imposed temperature and imposed heat flux at the lower wall are henceforth referred to as case (I) and case (II), respectively.

For case (I) we obtain $T(z) = -z$ for the liquid layer (with $0 \leqslant z \leqslant 1$) and $T(z) = \{(K/K_g)(1-z) - 1\}$ for the gas layer (with $1 \leqslant z \leqslant (1 + d_g/d)$). In these expressions, K and K_g stand for the thermal conductivities of the liquid and gas, respectively. For this case we determine $\Delta T_0^* = (T_b^* - T_i^*) = (T_b^* - T_t^*)/(1 + H^{-1})$ where $H = K_g d/K d_g$ is the static Biot number at the interface. For case (II) we obtain $\mathrm{d}T/\mathrm{d}z = -1$ for the liquid layer and $\mathrm{d}T/\mathrm{d}z = -(K/K_g)$ for the gas layer. In this case the temperature scale ΔT_0^* is determined to be $\Delta T_0^* = Q_0^* d/K$, and the upper wall temperature T_t^* provides the reference temperature.

We perturb the basic equations to obtain the disturbance equations, in which d, d^2/κ, κ/d, $\rho\nu\kappa/d^2$ and ΔT_0^* are introduced as the scales of length, time, velocity, pressure relative to the hydrostatic pressure, and temperature of the liquid and gas, respectively. In the scales, κ and ν are the thermal diffusivity and kinematic viscosity of the liquid, respectively. The liquid layer is assumed to be governed by the following forms of momentum and energy equations:

$$Pr^{-1}\partial_t \boldsymbol{v} = -\nabla p + \nabla^2 \boldsymbol{v} - Pr^{-1}\boldsymbol{v}\cdot\nabla\boldsymbol{v} + Ra\ \theta \boldsymbol{k}, \tag{2.1a}$$

$$\partial_t \theta = \boldsymbol{k}\cdot\boldsymbol{v} + \nabla^2\theta - \boldsymbol{v}\cdot\nabla\theta, \tag{2.1b}$$

and the gas layer by the heat conduction equation

$$\partial_t \theta_g = \left(\frac{\kappa_g}{\kappa}\right)\nabla^2\theta_g, \tag{2.1c}$$

where $\boldsymbol{v} = (u, v, w)$ denotes the perturbation velocity vector, θ is the perturbation temperature of the liquid, θ_g is the perturbation temperature of the gas and κ_g is the thermal diffusivity of the gas. The Prandtl number and Rayleigh number are defined, respectively, as $Pr = \nu/\kappa$ and $Ra = \alpha g \Delta T_0^* d^3/\nu\kappa$, where α is the coefficient of thermal expansion, g is acceleration due to gravity, and ΔT_0^* has been defined above for the two cases. The heat diffusion equation for θ_s, the perturbation temperature in the upper wall, is not considered. For the linear problem, the effects of finite conductivity of the upper wall can be incorporated in the boundary condition for θ_g (see Pérez-García *et al.* 1998). On the other hand, for the weakly nonlinear problem, we are primarily interested in a highly conducting upper wall which corresponds to the experimental condition of Schatz *et al.* (1995) where the Biot number for the wall was greater than 500, as we discuss later, so that the wall perturbation temperature was negligible.

The three-dimensional flow field is further constrained by the continuity equation

$$\partial_x u + \partial_y v + \partial_z w = 0, \tag{2.2}$$

and by appropriate boundary conditions given in (2.8) to (2.14) below. We now use the continuity equation to eliminate u and v in favour of w. The equation of motion (2.1a) and the energy equation (2.1b) can then be expressed in terms of only three variables w, θ and θ_g as

$$\mathscr{M}\begin{pmatrix} \partial_t w \\ \partial_t \theta \\ \partial_t \theta_g \end{pmatrix} = \mathscr{L}\begin{pmatrix} w \\ \theta \\ \theta_g \end{pmatrix} + \mathbf{N}. \tag{2.3}$$

The two linear differential operators are defined as

$$\mathscr{M} = \begin{bmatrix} Pr^{-1}(\nabla_\perp^2 + \partial_{zz}) & 0 & 0 \\ 0 & 1 & 0 \\ 0 & 0 & 1 \end{bmatrix}, \tag{2.4}$$

and

$$\mathscr{L} = \begin{bmatrix} (\nabla_\perp^2 + \partial_{zz})^2 & Ra\nabla_\perp^2 & 0 \\ 1 & (\nabla_\perp^2 + \partial_{zz}) & 0 \\ 0 & 0 & (\nabla_\perp^2 + \partial_{zz}) \end{bmatrix}, \tag{2.5}$$

and the nonlinear operator $\mathbf{N}$ depends on w and θ with its two components given

by $\mathbf{N} = (N_1, N_2, 0)^T$ (where $\boldsymbol{x}^T$ denotes the transpose of vector $\boldsymbol{x}$). The two nonlinear components are given by

$$N_1 = Pr^{-1}\{-\nabla_\perp^2((u\partial_x + v\partial_y + w\partial_z)w) + \partial_z \nabla_\perp \cdot ((u\partial_x + v\partial_y + w\partial_z)\boldsymbol{v}_\perp)\}, \tag{2.6}$$

$$N_2 = -(u\partial_x + v\partial_y + w\partial_z)\theta. \tag{2.7}$$

We have defined $\nabla_\perp^2$ equal to $(\nabla^2 - \partial_{zz})$ and $\boldsymbol{v}_\perp$ to be the horizontal velocity (u, v).

The lower wall ($z = 0$) is governed by the non-permeable and non-slip boundary conditions,

$$w(x, y, 0, t) = \partial_z w(x, y, 0, t) = 0. \tag{2.8}$$

The thermal condition here involves feedback. In both cases (I) and (II), we consider a sensor plane at the interface on which only the perturbation temperature $\theta(x, y, 1, t)$ is measured. In case (I) we have at the lower wall

$$\theta(x, y, 0, t) = \theta_c(x, y, t), \tag{2.9}$$

and in case (II) we have

$$\partial_z \theta(x, y, 0, t) = q_c(x, y, t), \tag{2.10}$$

where $q_c = (Q^*(x, y, t) - Q_0^*)/Q_0^*$; θ_c is a control temperature whereas q_c is a control heat flux. In addition, we assume a cubic feedback control law,

$$\left.\begin{array}{c}\theta_c(x, y, t) \\ \text{or} \\ q_c(x, y, t)\end{array}\right\} = -K_p\theta(x, y, 1, t) - K_q\theta^2(x, y, 1, t) - K_c\theta^3(x, y, 1, t), \tag{2.11}$$

where K_p, K_q and K_c are non-dimensional gains which are allowed to take various values for the two cases. Since the upper wall at $z = 1 + d_g/d$ is maintained at constant temperature, the boundary condition appropriate for θ_g there is

$$\theta_g = 0. \tag{2.12}$$

Because a non-deformable interface is assumed, the velocity and shear stress conditions at the interface ($z = 1$) are

$$w(x, y, 1, t) = \partial_{zz} w(x, y, 1, t) - Ma\nabla_\perp^2 \theta(x, y, 1, t) = 0. \tag{2.13}$$

The Marangoni number Ma is defined as $Ma = \gamma \Delta T_0^* d/\rho_0 \nu\kappa$ where $(-\gamma)$ is the derivative of surface tension with respect to temperature. The two fluid layers are thermally coupled through the interface. The continuity of temperature and heat flux provides two other equations at $z = 1$, namely,

$$\theta(x, y, 1, t) = \theta_g(x, y, 1, t), \quad \partial_z \theta(x, y, 1, t) = \left(\frac{K_g}{K}\right) \partial_z \theta_g(x, y, 1, t). \tag{2.14}$$

The perturbation procedure leading to the cubic-order amplitude equation is fairly standard (e.g. see Bestehorn 1993; Cloot & Lebon 1984; and Bragard & Velarde 1998 for the BM situation). The difference here is that we have included a massless and inviscid gas layer and a rigid conductive wall above it, along with the effects of feedback control. We perturb the governing equations about a critical onset condition given by $Ma = Ma_c$ and $Ra = Ra_c$. A schematic is given in figure 2. Since both Ma and Ra are proportional to ΔT_0^*, we consider the experimental situation in which both Ma and Ra vary along a physical line defined by $Ma = \Gamma Ra$ (see Bestehorn 1993, 1994; Echebarria & Pérez-García 2000). The value of Γ can be changed by

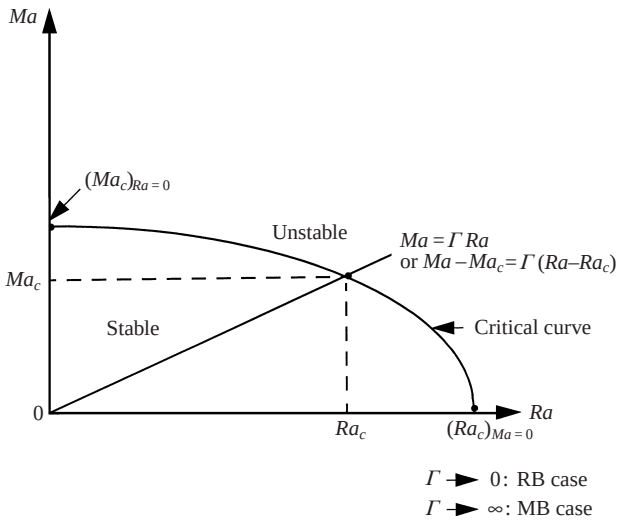

FIGURE 2. A schematic for Nield's stability diagram.

varying the layer thickness but Ma and Ra vary simultaneously for constant Γ by changing ΔT_0^*. For a small perturbation about the critical point, we now consider $\epsilon^{1/2}$, defined as $\epsilon^{1/2} = |Ma - Ma_c|/Ma_c = |Ra - Ra_c|/Ra_c$, as a scaling parameter for the perturbation scheme. The time and length variables are scaled according to

$$\partial_t = \epsilon^{1/2}\partial_{T_1} + \epsilon\partial_{T_2} + \cdots, \tag{2.15}$$

and

$$\nabla = \nabla_\perp + \boldsymbol{k}\partial_z + \epsilon^{1/2}\nabla_X, \tag{2.16}$$

where $\nabla_X = \partial_X \boldsymbol{i} + \partial_Y \boldsymbol{j}$. The stretched time and spatial variables are defined as $T_1 = \epsilon^{1/2}t$ and $T_2 = \epsilon t$, and $(X, Y) = \epsilon^{1/2}(x, y)$. Tang & Bau (1994) observed for RB convection that, when K_p is sufficiently high, oscillatory instability will occur. In this study, we assume for the weakly nonlinear analysis that K_p is such that monotonic instability occurs initially at a finite wavelength; the above scaling is then appropriate. The dependent variables for the fluid layer are expanded as follows:

$$\boldsymbol{v}_\perp = \epsilon^{1/2}\boldsymbol{v}_1 + \epsilon\boldsymbol{v}_2 + \cdots, \quad w = \epsilon^{1/2}w_1 + \epsilon w_2 + \cdots, \tag{2.17a,b}$$

$$\theta = \epsilon^{1/2}\theta_1 + \epsilon\theta_2 + \cdots, \quad \theta_g = \epsilon^{1/2}\theta_{g1} + \epsilon\theta_{g2} + \cdots, \tag{2.17c,d}$$

and Ma and Ra as

$$Ma = Ma_c + \epsilon^{1/2}Ma_1 + \epsilon Ma_2 + \cdots, \tag{2.17e}$$

$$Ra = Ra_c + \epsilon^{1/2}Ra_1 + \epsilon Ra_2 + \cdots\ . \tag{2.17f}$$

Note that Ma and Ra are constrained by the operating condition. Thus, since $Ma = \Gamma Ra$, we have $Ma_c = \Gamma Ra_c$, $Ma_i = \Gamma Ra_i$ for $i = 1, 2, \ldots$. Upon expansion, for case (I) the control law yields the following equations if we for the moment suppress the slow variables:

$$\theta_1(x, y, 0, t) + K_p\theta_1(x, y, 1, t) = 0, \tag{2.17g}$$

$$\theta_2(x, y, 0, t) + K_p\theta_2(x, y, 1, t) = -K_q\theta_1^2(x, y, 1, t) \tag{2.17h}$$

and

$$\theta_3(x,y,0,t)+K_p\theta_3(x,y,1,t)=-2K_q\theta_1(x,y,1,t)\,\theta_2(x,y,1,t)-K_c\theta_1^3(x,y,1,t). \tag{2.17i}$$

On the other hand, for case (II) the control law yields

$$\partial_z\theta_1(x,y,0,t)+K_p\theta_1(x,y,1,t)=0, \tag{2.17j}$$

$$\partial_z\theta_2(x,y,0,t)+K_p\theta_2(x,y,1,t)=-K_q\theta_1^2(x,y,1,t) \tag{2.17k}$$

and

$$\partial_z\theta_3(x,y,0,t)+K_p\theta_3(x,y,1,t)=-2K_q\theta_1(x,y,1,t)\theta_2(x,y,1,t)-K_c\theta_1^3(x,y,1,t) \tag{2.17l}$$

instead. The linear problem determines the values of Ma and Ra for neutral stability as a function of k and, in particular, the critical values Ra_c, Ma_c and k_c which will be given in § 3.

The linear solution is of $O(\epsilon^{1/2})$. A solution of the coupled problem of the two layers is sought in the following form:

$$w_1=f(z)\,\phi(x,y,t),\quad \theta_1=g(z)\,\phi(x,y,t),\quad \theta_{g1}=h(z)\,\phi(x,y,t). \tag{2.18}$$

Both $f(z)$ and $g(z)$ are defined for $0\leqslant z\leqslant 1$, whereas $h(z)$ is defined for $1\leqslant z\leqslant(1+d_g/d)$. It is more convenient to normalize w_1 than θ_1 since θ_1 is typically an order or more smaller in magnitude than w_1. Here we let $\int_0^1 f(z)\,\mathrm{d}z=1$. The horizontal planform function ϕ satisfies $\nabla_\perp^2\phi=-k_c^2\phi$ but the planform is not determined at this order.

The three most common planforms that have been considered theoretically are hexagons, rolls and squares. When subcriticality occurs, the hexagonal planform is stable near the onset but then, as the criticality parameter increases in, say, an experiment on BM convection, pentagonal and square patterns also occur; see Schatz *et al.* (1999). For RB convection without control, a supercritical bifurcation to rolls occurs but, as shown by Shortis & Hall (1996), the use of control promotes a subcritical instability in the form of hexagons. Here, we restrict the discussion to hexagons and concentrate on the onset of convection.

For these two planforms, we let

$$\phi=Ae_1+Be_2+Ce_3+\text{c.c.}, \tag{2.19}$$

where A, B and C are functions of the slow variables and c.c. denotes the complex-conjugate terms. The three basis functions are $e_j=\mathrm{e}^{\mathrm{i}\boldsymbol{k}_j\cdot\boldsymbol{r}_\perp}$ $(j=1,2,3)$, where $\boldsymbol{r}_\perp=(x,y)$. The three wavevectors are $\boldsymbol{k}_1=k_c(1/2,-\sqrt{3}/2)$, $\boldsymbol{k}_2=k_c(1/2,\sqrt{3}/2)$, and $\boldsymbol{k}_3=k_c(-1,0)$ so that $k_1+k_2+k_3=0$.

In the numerical procedure, all the functions corresponding to the vertical dependence, such as $f(z)$, $g(z)$, and $h(z)$, are computed from the governing o.d.e.s in terms of Chebyshev polynomials and the boundary conditions are incorporated by the tau method. At $O(\epsilon)$, the governing equations have non-homogeneous terms arising from nonlinearity as well as terms reflecting change with respect to T_1. By averaging the equations with the adjoint solution, a solvability condition can be obtained that gives rise to the following set of amplitude equations:

$$\tau\begin{pmatrix}\partial_{T_1}A\\ \partial_{T_1}B\\ \partial_{T_1}C\end{pmatrix}=\begin{pmatrix}(s_mMa_1+s_rRa_1)A+q_1\overline{B}\,\overline{C}\\ (s_mMa_1+s_rRa_1)B+q_1\overline{A}\,\overline{C}\\ (s_mMa_1+s_rRa_1)C+q_1\overline{A}\,\overline{B}\end{pmatrix} \tag{2.20}$$

where s_m, s_r and q_1 are evaluated numerically. The equilibria defined by the steady form

of (2.20) correspond to specific values of Ma_1 and Ra_1. After obtaining the solutions for w_2, θ_2 and θ_{g2}, we proceed to $O(\epsilon^{3/2})$ where additional non-homogeneous terms occur due to nonlinearity, the additional slow variables and a possible offset of the wavenumber from the critical value. Allowing A, B and C to depend on X, Y and T_2, a second set of amplitude equations can be obtained via a solvability condition; it can be expressed as

$$\tau\begin{pmatrix}\partial_{T_2}A\\ \partial_{T_2}B\\ \partial_{T_2}C\end{pmatrix}=\begin{pmatrix}(s_mMa_2+s_rRa_2)+\xi_1(\boldsymbol{k}_1\cdot\nabla_X)^2+\xi_2\nabla_X^2)A-g_p|A|^2A\\ (s_mMa_2+s_rRa_2)+\xi_1(\boldsymbol{k}_2\cdot\nabla_X)^2+\xi_2\nabla_X^2)B-g_p|B|^2B\\ (s_mMa_2+s_rRa_2)+\xi_1(\boldsymbol{k}_3\cdot\nabla_X)^2+\xi_2\nabla_X^2)C-g_p|C|^2C\end{pmatrix}$$

$$\begin{pmatrix}-g_c(|B|^2+|C|^2)A+\mathrm{i}\beta_1(\overline{B}\boldsymbol{k}_3\cdot\nabla\overline{C}-\overline{C}\boldsymbol{k}_2\cdot\nabla\overline{B})+\mathrm{i}\beta_2(\overline{C}\boldsymbol{k}_3\cdot\nabla\overline{B}-\overline{B}\boldsymbol{k}_2\cdot\nabla\overline{C})\\ -g_c(|A|^2+|C|^2)B+\mathrm{i}\beta_1(\overline{A}\boldsymbol{k}_3\cdot\nabla\overline{C}-\overline{C}\boldsymbol{k}_1\cdot\nabla\overline{A})+\mathrm{i}\beta_2(\overline{C}\boldsymbol{k}_3\cdot\nabla\overline{A}-\overline{A}\boldsymbol{k}_1\cdot\nabla\overline{C})\\ -g_c(|A|^2+|B|^2)C+\mathrm{i}\beta_1(\overline{A}\boldsymbol{k}_2\cdot\nabla\overline{B}+\overline{B}\boldsymbol{k}_1\cdot\nabla\overline{A})+\mathrm{i}\beta_2(\overline{A}\boldsymbol{k}_1\cdot\nabla\overline{B}+\overline{B}\boldsymbol{k}_2\cdot\nabla\overline{A})\end{pmatrix} \tag{2.21}$$

where g_p, g_c, ξ_1 and ξ_2 are also determined numerically via the solvability condition, and β_1 and β_2 are further numerical constants associated with the expansion of the nonlinear terms by Chebyshev polynomials.

The two solvability conditions can be combined to yield a single set of amplitude equations. We rescale the amplitudes according to

$$\epsilon^{1/2}A=a(t)\,\mathrm{e}^{\mathrm{i}\tilde{K}\boldsymbol{k}_1\cdot\boldsymbol{r}_\perp},\quad \epsilon^{1/2}B=b(t)\,\mathrm{e}^{\mathrm{i}\tilde{K}\boldsymbol{k}_2\cdot\boldsymbol{r}_\perp},\quad \epsilon^{1/2}C=c(t)\,\mathrm{e}^{\mathrm{i}\tilde{K}\boldsymbol{k}_3\cdot\boldsymbol{r}_\perp} \tag{2.22}$$

where $a(t)$, $b(t)$ and $c(t)$ are real and $\tilde{K}$ satisfies $k=k_c(1+\epsilon^{1/2}\tilde{K})$. After rescaling (2.20), (2.21) and adding the resulting two sets of equations, we have a single set of equations. By varying Ma and Ra simultaneously along the operating condition $Ma=\Gamma Ra$, we require $(Ma-Ma_c)/Ma_c=(Ra-Ra_c)/Ra_c$ when $0<\Gamma<\infty$ which we denote as $\hat{\epsilon}$. In the limits $Ra\to Ra_c$ or $Ma\to Ma_c$, however, we define $\hat{\epsilon}=(Ma-Ma_c)/Ma_c$ or $\hat{\epsilon}=(Ra-Ra_c)/Ra_c$. We add (2.20), (2.21) and use (2.17e, f) to obtain the set of equations

$$\tau_0\begin{pmatrix}\partial_t a\\ \partial_t b\\ \partial_t c\end{pmatrix}=\begin{pmatrix}\hat{\epsilon}a+qbc-\hat{g}_pa^3-\hat{g}_c(b^2+c^2)a\\ \hat{\epsilon}b+qac-\hat{g}_pb^3-\hat{g}_c(a^2+c^2)b\\ \hat{\epsilon}c+qab-\hat{g}_pc^3-\hat{g}_c(a^2+b^2)c\end{pmatrix}. \tag{2.23}$$

The operating parameter $\hat{\epsilon}$ represents the deviations of Ma and Ra from Ma_c and Ra_c, respectively, as well as k from k_c; it is given by

$$\hat{\epsilon}=-\xi\tilde{k}^2+\frac{1}{S}(\epsilon^{1/2}(s_mMa_1+s_rRa_1)+\epsilon(s_mMa_2+s_rRa_2)+\cdots), \tag{2.24}$$

where $S=(s_mMa_c+s_rRa_c)$, $\tilde{k}=k-k_c$ and $\xi=\xi_1+\xi_2$ and $\tau_0=\tau/S$. For an alternative derivation leading to the standard-form amplitude equation (2.23), we refer to Echebarria & Pérez-García (2000). The quadratic-term coefficient q is given by

$$q=(q_1+(\beta_2-2\beta_1)k_c\tilde{k})/S. \tag{2.25}$$

We have rescaled the coefficients g_p and g_c by S and then let $\hat{g}_p$ and $\hat{g}_c$ denote g_p/S and g_c/S, respectively. The form of the amplitude equations for the uncontrolled case is preserved under the controlled situation. The linear control gain K_p affects all the

coefficients by distorting the mode shape. The quadratic gain K_q does not affect $\hat{\epsilon}$ but affects q, g_p and g_c, and K_c affects g_p and g_c.

3. Results

3.1. *RBM convection without feedback control*

It is possible to solve the linear problem by eliminating the dependent variable θ_g. This simplification can be achieved for monotonic disturbances for which the growth rate is $O(\epsilon)$. By solving $\nabla^2\theta_g = 0$ explicitly and using the upper wall boundary condition, the interfacial boundary condition gives

$$\partial_z\theta + Bi_{eff}\theta = 0, \tag{3.1}$$

where $Bi_{eff}(k)$ is the effective Biot number given by

$$Bi_{eff}(k) = (K_g/K)k \coth(kd_g/d). \tag{3.2}$$

Since $k_c \sim O(1)$, $Bi_{eff} \to (K_g d/K d_g)$ when $d_g \ll d$, but, when $d_g \gg d$, $Bi_{eff} \to k_c(K_g/K) \approx 0$ when $K_g \ll K$.

We start by checking our linear results against some known calculations. We note that if Bi_{eff} is considered as a constant parameter, then the classical one-layer model is recovered, with a mixed free-surface thermal boundary condition. In this case, our results reproduce Nield's tabulated critical values for Biot number with good accuracy (agreement with the results in table 1 of Nield (1964) to at least two decimal places). On the other hand, if we use the experimental parameters $K_g/K = 0.204$ and $d_g/d = 1.086$ according to the experiment of Schatz *et al.* (1995), our neutral curve of Ma versus k with $Ra = 0$ agrees with the result from (29) of Pérez-García *et al.* (1998).

We now compare the critical parameters to the experimental results of Schatz *et al.* (1995) corresponding to case (I) only. For the purpose of comparison, we use the material properties and physical dimensions of the experiment. The upper wall of their apparatus is a sapphire window. On the basis of private communication with Professor Schatz, we use $d_s = 0.1\,\text{cm}$ and $K_s = 0.35\,\text{W}\,\text{cm}^{-1}\,^\circ\text{C}^{-1}$. In the experiment, T_t^* is the basic temperature of the reservoir containing cooling water in contact with the upper surface of the sapphire window and not the temperature at the upper boundary of the gas. So ΔT_0 is smaller than the infinitely conductive value. However, we found the reduction factor due to finite conductivity to be $(1+H^{-1})/(1+H^{-1}+H_s^{-1})$ where $H_s = K_s d/K d_s$; this factor has a value of about 0.996. The corresponding Biot number for the upper wall is $Bi_s = K_s d/K_g d_s = 575.1$. For such a large value, the assumption of an infinitely conductive upper wall seems justified.

The correction due to the finite conductivity of the gas layer was discussed by Pérez-García *et al.* (1998). If $\Gamma = 40$ is used in our model, the critical values for case (I) are $k_c = 1.99$, $Ma_c = 95.38$ and $Ra_c = 2.38$, and, for case (II), $k_c = 1.16$, $Ma_c = 67.90$ and $Ra_c = 1.70$. From (3.2) we obtain $Bi_{eff} = 0.42$ and 0.28, respectively, for the two cases. Both Ra_c and Ma_c of case (I) agree reasonably well with the tabulated results of Pérez-García *et al.* (1998, table II), except that the authors obtained $k_c = 1.97$ which is slightly smaller. The finite upper-wall effect will decrease Ma_c by 0.4%, which is probably of the magnitude of experimental uncertainties. In the experiment reported by Schatz *et al.* (1995), the critical values were given as $k_c \approx 1.90$ and $Ma_c \approx 83.6$. In the later experiment reported by Schatz *et al.* (1999), however, only theoretical values of the critical parameters were reported,

which agree with our values to within 1%. But the discrepancy between the measured and theoretical critical values remained unresolved. In recent work, Regnier *et al.* (2000) have shown that interfacial deformation is destabilizing in the thermocapillary regime (corresponding to large values of Γ with our definition of Γ). This aspect of the problem needs further investigation.

The subcritical hysteresis was reported in detail by Schatz *et al.* (1995). It seems that the degree of hysteresis is independent of the exact value of Ma_c, since the ϵ used in the experiment is a scaled parameter. In order to provide a comparison, we obtain a single amplitude equation such as the one used by Schatz *et al.* (1995). We consider $a = b = c$ for the hexagonal solution and obtain

$$\tau_0 \partial_t a = (\hat{\epsilon} - \xi \tilde{k}^2)a + qa^2 - ga^3, \tag{3.3}$$

where

$$g = (g_p + 2g_c). \tag{3.4}$$

The parameter $\hat{\epsilon}_N$ measures the subcritical hysteresis, defined as $(Ma_N - Ma_c)/Ma_c$, where Ma_N is the minimum value of the subcritical range, referred to as the turning point or 'nose'. From (3.3) we obtain $\hat{\epsilon}_N = -q^2/4g$.

Before comparing with the experiment, we note that the theoretical results for hysteresis published so far correspond to the single-layer model with a fixed value of Bi_{eff} (case I only). The case $Bi_{eff} = 0$ has been investigated by a number of authors. In this limit we obtain critical values of $Ma_c = 79.607$ and $k_c = 1.998$, in agreement with the well-known linear result. At $k = k_c$, the coefficients of (3.3) are evaluated to be

$$\left.\begin{aligned} \tau_0 = 0.17 + 0.043Pr^{-1}, \quad \xi = 0.29, \quad q = (0.49 - 0.11Pr^{-1}) + (1.24 - 0.30Pr^{-1})\tilde{k}, \\ g = 10.40 + 1.50Pr^{-1} - 0.39Pr^{-2}. \end{aligned}\right\} \tag{3.5}$$

For $Pr = \infty$, the hysteresis is found to be $\hat{\epsilon}_N = -0.58\%$. The most recent discussion on the value of $\hat{\epsilon}_N$ value is by Echebarria & Pérez-García (2001) who have compared the values obtained by several authors. According to their summary, $\hat{\epsilon}_N$ lies in the range between -0.56 and -0.8. Other authors whose results were not included in the summary but who have also computed this subcritical hysteresis are Bestehorn (1994) and Bragard & Velarde (1998). Their values fall within the same range. In this classical case, a change in the nature of hexagons from the ℓ-type to the g-type as Pr decreases was first reported by Thess & Bestehorn (1995) and then by Bragard & Velarde (1998). Our numerical solutions also show that a transition occurs at $Pr \approx 0.22$, which agrees with the value found by Thess & Bestehorn (1995; see their figure 3 for $Bi = 0$).

Now, we consider the material properties and physical conditions specified in the original experiment by Schatz *et al.* (1995). We use $Pr = 82.6$ for silicone oil. For case (I) our result yields

$$\left.\begin{aligned} \tau_0 = 0.15 + 0.043Pr^{-1}, \quad \xi = 0.29, \quad q = (0.49 - 0.11Pr^{-1}) + (1.24 - 0.30Pr^{-1})\tilde{k}, \\ g = 8.04 + 1.60Pr^{-1} - 0.40Pr^{-2}. \end{aligned}\right\} \tag{3.6}$$

From our theoretical result, the hysteresis is $\hat{\epsilon}_N = -0.74\%$. Thus, the hysteresis based on the minimal two-layer model is about 28% larger than the value of the case with $Bi_{eff} = 0$. To compare case (I) and case (II), we consider the same K_g/K, κ_g/κ and d_g/d of the original experiment. These values are, respectively, 0.2, 241.9 and 1.09.

Our result for case (II) yields

$$\left.\begin{aligned}\tau_0 = 0.60 + 0.048Pr^{-1}, \quad \xi = 0.76, \quad q = (0.61 - 0.13Pr^{-1}) - (0.38 + 0.12Pr^{-1})\tilde{k},\\ g = 27.74 + 7.47Pr^{-1} - 1.71Pr^{-2}.\end{aligned}\right\} \tag{3.7}$$

The hysteresis for case (II) gives $\hat{\epsilon}_N = -0.31\%$, which is about 40% of the value of case (I).

The theoretical hysteresis for case (I), $\hat{\epsilon}_N = -0.74\%$, is too small to match the measured hysteresis value of about -3.2% reported in Schatz *et al.* (1995). We further note that a change in the hysteresis can occur due to a shift of wavenumber from the critical value. It is well-known that there is a finite Eckhaus band of wavenumber within which the steady solution is stable. In the experiment the measured spectral peak of wavenumber appeared to be about $k = 1.90$. Since the small shift of $\delta k \approx -0.09$ is well within the Eckhaus limit for the range of $\hat{\epsilon}$ considered in the experiment, it seems that a larger-wavelength convection pattern than characterized by the critical wavelength is realized in the experiment. As seen in (2.23), the wavenumber shift will contribute to the quadratic coefficient q, thereby affecting the subcritical hysteresis. But this correction turns out to decrease $|\hat{\epsilon}_N|$ rather than to increase it. For $\tilde{k} = -0.09$, we obtain $\hat{\epsilon}_N = -0.61$, which is even smaller in magnitude than the value at the critical wavelength.

The effects of temperature-dependent viscosity have not been included in our model for simplicity. In fact, these effects are relatively small. In the experiment of Schatz *et al.* (1995), the temperature difference across the liquid is about $\sim 1.65\,^{\circ}\mathrm{C}$, and an estimation of the variation of ν with temperature for purified silicone oils can be obtained from Wilcock (1946) as $(\mathrm{d}\nu/\mathrm{d}T)_{T_0} \approx -10^{-3}$, so $\gamma = \Delta T(\mathrm{d}\nu/\mathrm{d}T)_{T_0}/\nu_0 \approx -0.0232$. With variable viscosity for the one-layer model at infinite Pr, we obtain $Ma_c = 79.89$, a 0.35% increase, since the region near the free surface where thermocapillarity drives the flow is now more viscous. On the other hand, hysteresis is stronger at $\epsilon_N = -0.58$, a 1.4% increase in magnitude. The increase is in the direction of reducing the discrepancy, but like the other factors considered above, it is too small to account for the large discrepancy. It should also be mentioned that the recent work of Regnier *et al.* (2000) indicates that surface deformation tends to decrease the amount of hysteresis for hexagons in the thermocapillary regime instead of increasing it; see their figure 6.

From a theoretical point of view, it is worthwhile to see how sensitive the subcritical hysteresis is to changes in conditions. Of particular interest is the dependence of the critical parameters and the hysteresis on the relative layer thickness d_g/d. We investigate this relationship for both case (I) and case (II). Since the buoyancy effect is minor if d is assumed to be small, we consider the case $Ra = 0$ for simplicity. We let K_g/K and κ_g/κ have the experimental specifications but consider the gas layer thickness to vary. In figure 3(a, b), we show the curves of critical wavenumber k_c and Marangoni number Ma_c versus d_g/d. The results are based on a constant $Bi_s = 575.1$. The solid and dashed curves correspond to case (I) and case (II), respectively. For case (I), the solid line of figure 3(b) agrees quite well with the lower solid curve of figure 5 of Pérez-García *et al.* (1998). For $d_g/d \gg 1$, Ma_c approaches a value slightly below 100 but Ma_c increases as d_g/d decreases towards zero. Both our results and those of Pérez-García *et al.* (1998) predict $Ma_c \approx 122$ at $d_g/d = 0.2$. For case (II), both k_c and Ma_c are consistently lower than those of case (I) but the trend remains similar except that for case (II) as d_g/d becomes larger (implying that Bi_{eff} decreases)

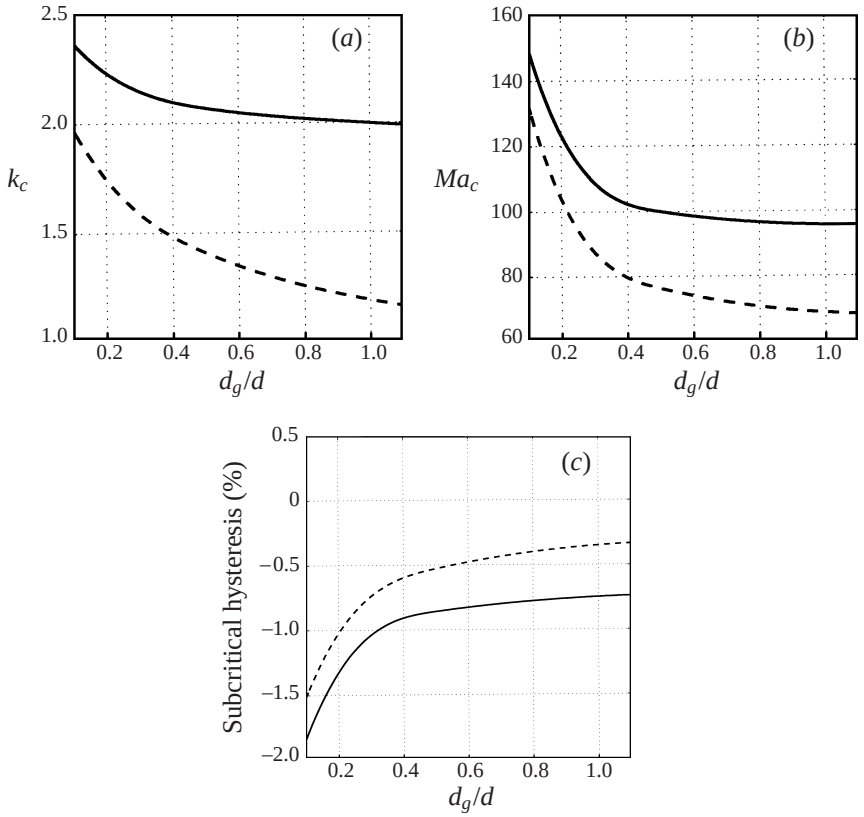

FIGURE 3. The variation of (*a*) critical wavenumber, (*b*) critical Marangoni number and (*c*) subcritical hysteresis ($\hat{\epsilon}_N$), with the depth ratio d_g/d in the two-layer model with $Pr = 82.6$, $Ra = 0$ and $\tilde{k} = 0$ and $Bi_s = 575.1$. The solid and dashed lines correspond to case (I) and (II), respectively.

we observe that k_c becomes small. The current analysis is not applicable to $k_c \to 0$ due to the scalings. In figure 3(*c*) we show the hysteresis $\hat{\epsilon}_N$ for the two cases. The subcritical hysteresis is significantly stronger when $d_g \ll d$ but then it tends to about -0.72% for case (I) when $d_g/d \to \infty$. The hysteresis is weaker for case (II). Except for the trend of k_c for case (II), the results indicate that change with d_g/d is very gradual for $d_g/d > 0.5$. The trend of increase of $|\hat{\epsilon}_N|$ with decrease of d_g/d appears to be consistent with that of a one-layer model, if Bi_{eff} is estimated based on d_g/d. We are able to reproduce Bestehorn's result (1994, see his figure 3), which shows that $|\hat{\epsilon}_N|$ increases with Biot number. The limit $d_g/d \to \infty$ corresponds to $Bi_{eff} = 0$. For finite d_g/d let us consider a point at $d_g/d = 0.2$ (see figure 2(*c*), solid curve). At this depth ratio we obtain $Bi_{eff} \approx 1.09$. The one-layer model at this value gives $|\hat{\epsilon}_N| = 1.24\%$, which clearly shows an increase from the value of 0.58% at $Bi_{eff} = 0$. The corresponding value from the two-layer model is slightly larger, at 1.3%. We note that some experimental data on the variation of hysteresis with the depth ratio were published recently by Kang & Hu (1999). However, a comparison reveals that their data exhibit an opposite trend to our theoretical results, namely $|\hat{\epsilon}_N|$ decreases rather than increases as d_g/d decreases.

We remark that if the gas and upper wall have comparable conductivities, then the upper thermal boundary condition for the gas layer is not strictly valid. In other words, we cannot assume a constant Biot number Bi_s. Even using $Bi_s(k)$ according

to $Bi_s(k) = (K_s/K_g)k\coth(kd_s/d)$ is valid only for the linear problem. In general, we have to consider the upper wall as a separate conductive layer.

3.2. *RBM convection with feedback control*

Now we apply feedback control to the fluid layer. In order for the linear theory to be valid, the initial disturbance state to be controlled has to be maintained at infinitesimal amplitude. This condition can be achieved in an environment with a low ambient disturbance level by slowly increasing Ma and Ra. Furthermore, since an oscillatory instability will presumably occur when K_p is sufficiently large, we anticipate that the stable region of the basic state is bounded by a transition curve to the oscillatory mode. Since our weakly nonlinear problem is formulated strictly for the monotonic mode, the weakly nonlinear oscillatory solution is beyond our scope. Nevertheless, the linear characteristics of the oscillatory instability are of interest and will be briefly discussed below. A boundary curve which marks the transition to the oscillatory instability will be constructed in the (Ra, Ma)-plane.

For case (I) the insulated case corresponding to $Bi_{eff} = 0$ is considered first, followed by the two-layer configuration. The insulated case is a relatively simple situation that has been considered by numerous authors for the uncontrolled problem. For case (II), it is pertinent to have a comparison with case (I) using the parameters of the experiment by Schatz *et al.* (1995).

The effect of stabilization of the basic state in terms of the proportional gain K_p for a single-layer configuration with $Ra = 0$ has been obtained by Bau (1999). We compared our results with figure 1 of Bau (1999) as a numerical check, and the agreement is good. With both Ra and Ma non-zero, the stability is now predicted according to Nield's description. In order to determine the critical values (the minimum of $Ra(k)$ and $Ma(k)$ on the (Ra, Ma)-plane), we vary both parameters along the physical line defined by $Ma(k) = \Gamma\, Ra(k)$. The stability diagrams for case (I) corresponding to the insulated case $Bi_{eff} = 0$ and the two-layer model (with K_g/K and d_g/d corresponding to the experimental values) are shown in figures 4(a) and 4(b), respectively. The stability diagram for case (II) (two-layer only) is shown in figure 4(c). In the stability diagrams the solid lines represent the critical curves for monotonic onset. These curves are Prandtl-number independent. For all three cases, Nield's line ($K_p = 0$) can be approximated well by a straight line $Ma_c/Ma_{c0} + Ra_c/Ra_{c0} = 1$. With feedback control we consider moderate values of K_p. In figure 4(a, b), we show two critical curves for $K_p = 2$ and 5. In figure 4(c), we show only one control case, corresponding to $K_p = -5$. As $|K_p|$ increases, the critical curves shift outward. The slope of the curve also changes with K_p, as clearly indicated in figure 4(a, b). Unlike the curves for lower $|K_p|$, the critical curve at $K_p = 5$ intersects a limiting curve (dashed line). Beyond this intersection the solid line no longer represents the critical curve and therefore this outer portion is not shown.

For case (II), figure 4(c) shows similar qualitative behaviour to the two other cases but higher values of K_p are necessary to induce oscillations. With boundary condition (2.10), with q_c as given by (2.11), we found that $K_p > 0$ is destabilizing while $K_p < 0$ is stabilizing for this case. It should be noted that $K_p < 0$ corresponds to a reduced (increased) heat flux at the lower wall below a positive (negative) interfacial perturbation temperature.

In figures 4(a)–4(c), the dashed curve is the transition curve corresponding to the onset of oscillatory instability, which puts a bound on the largest value of K_p that we can use with feedback control. For a given point (Ra, Ma) on the plane below the dashed curve, we can always find a K_p value to stabilize the basic state. The K_p value

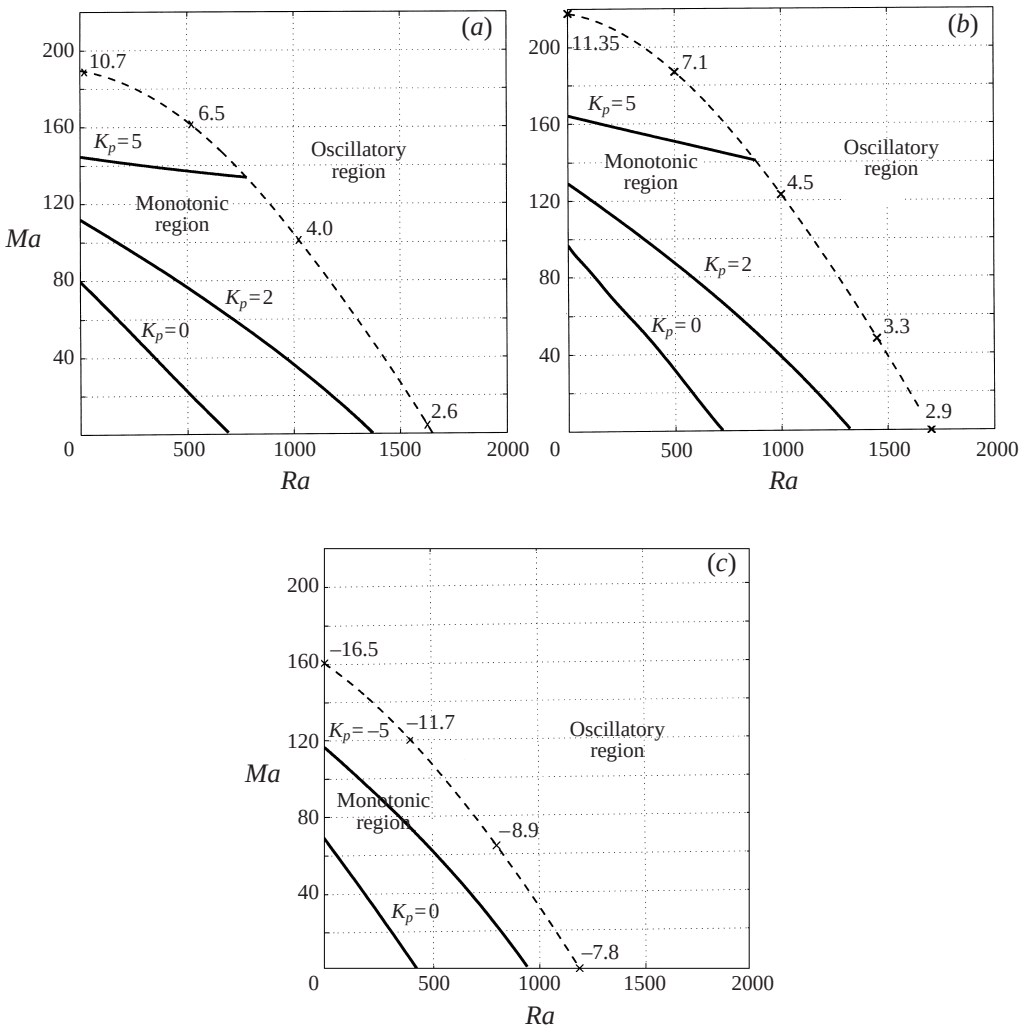

FIGURE 4. (*a*) Stability diagram for case (I): insulating interace $Bi_{eff} = 0$. The three critical solid curves correspond to $K_p = 0$, 2 and 5. The dashed line is the critical curve for the onset of the oscillatory instability. The numbers along the curve mark the values of K_p. (*b*) Stability diagram for case (I): the two-layer model. (*c*) Stability diagram for case (II): the two-layer model.

varies along the dashed curve, as shown by the numbers labelling the cross-signs. This curve is computed on the condition that both the monotonic and oscillatory modes simultaneously cross the zero growth rate. Unlike the solid curves, the dashed curves depend on Pr; all three cases of figures 4(*a*)–4(*c*) are computed at $Pr = 82.6$.

In order to explain the transition to the oscillatory instability, we consider the pair of eigenvalues closest to the neutral stability condition and show how they vary with K_p. Consider BM convection ($Ra = 0$) at $Pr = 82.6$, $Ma = 160$ and $k = 3.0$ for case (I). Figures 5(*a*) and 5(*b*) show, respectively, the real part (growth rate) and imaginary part (frequency) of the pair of eigenvalues. At $K_p = 0$, the two growth rates correspond to the first and second monotonic modes. As K_p increases, the control action tends to stabilize the unstable mode at the expense of destabilizing the second mode, which is stable without control. A coalescence occurs for $K_p \approx 7.8$.

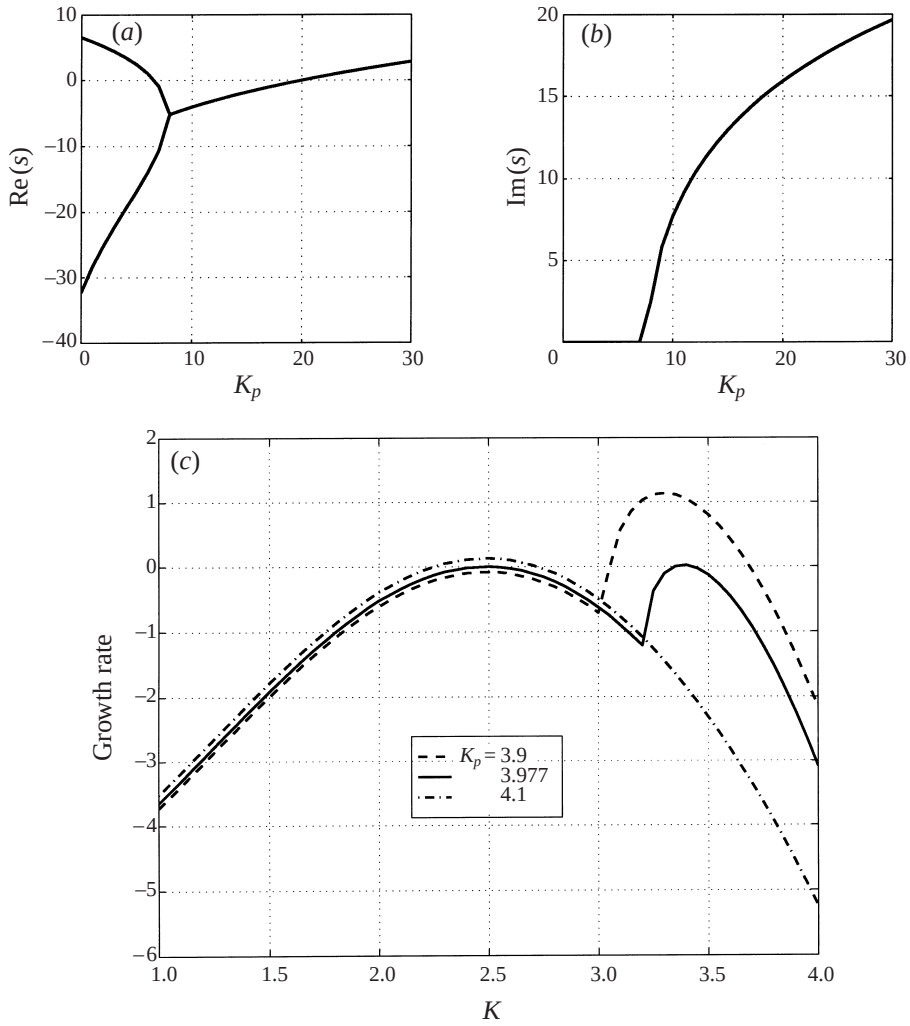

FIGURE 5. The variation with K_p of (*a*) the real part and (*b*) the imaginary part of the least stable pair of eigenvalues for $Pr = 82.6$, $Ma = 160$, $Ra = 0$ and $k = 3$. (*c*) The real part of the least stable eigenvalue versus k for three values of K_p near a point on the dashed curve of figure 4.

Beyond this gain the least stable mode is oscillatory. When K_p is sufficiently large, this mode becomes unstable, as indicated by the dashed curves in figure 4(*a*, *b*). This phenomenon explains the origin of the oscillatory instability at large gain. One can vary either Ma or Ra along the line $\Gamma = \text{constant}$ (for $\Gamma \neq 0, \infty$). By varying K_p at the same time one can obtain the growth rate as a function of k and note that two maxima can cross zero to become positive simultaneously. In figure 5(*c*), we show the growth rate versus k at a point near the limiting curve $(Ra_c, Ma_c) = (1018, 101.8)$. The solid curve corresponds to $K_p = 3.977$, which indicates a double maxima of growth rate near $k = 2.5$ (oscillatory mode) and $k = 3.35$ (monotonic mode). The dashed curve shows the shift of growth rate versus k when K_p is slightly smaller. In this case, the monotonic mode has a stronger growth rate. The dashed-dotted curve corresponds to a larger K_p, for which the oscillatory mode already dominates.

Now, going back to figures 4(*a*) to 4(*c*), the maximum stabilization in each case

corresponds to the dashed curve. For both BM and RB limits, the critical value with maximal control is between 2 to 2.5 times its uncontrolled value. The extension of stabilization for RB and BM convection is roughly the same. We observe that the mode shapes for the two cases are similar. Since the sensor for both cases is located at a level of maximum thermal perturbation and the actuator for both cases is located at the lower wall, the feedback affects both cases in a similar manner. The critical wavenumbers of BM and RB convection at the dashed curve are approximately the same for cases (I) and (II). For the monotonic mode, k_c is between 3.4 and 3.6 for BM convection and is slightly larger for RB convection. For the oscillatory mode, k_c is about 2.6 for BM convection and 1.5 for RB convection. As mentioned already, the dashed curves in figures 4(*a*)–4(*c*) depend on Pr and are computed at $Pr = 82.6$. By decreasing Pr to 7.0, the change in the critical Ra or Ma in any case is found to be less than 3%.

For case (I) of uncontrolled RBM convection, Bestehorn (1994) showed the variation of the subcritical hysteresis along the Nield curve. The hysteresis has a maximum in the BM limit but then decreases in amplitude monotonically to zero in the RB limit. In the BM limit, convection is realized as ℓ-type hexagons. When feedback control is applied, the feedback produces a distortion of the disturbance field that can reinforce or weaken this subcritical instability. In RB convection, where subcritical instability is absent in the uncontrolled case, Shortis & Hall (1996) reported that the feedback control induces subcritical g-type hexagons for small values of K_p. We consider the dependence of the subcritical hysteresis for the range of K_p values prior to the onset of oscillatory instability, for both cases (I) and (II) and in both the RB and BM limits. The results are shown in figures 6(*a*)–6(*d*). For case (I) with $Bi_{eff} = 0$ in the BM limit, figure 6(*a*) (thin lines) shows the hysteresis for K_p between 0 and 10.7. The monotonic solution is preferred for $K_p < 10.7$. In this range, k_c increases from 1.99 to 3.58 whereas Ma_c increases from 79.6 to 189.5 due to the stabilizing effects. The hysteresis decreases to zero and then increases somewhat. The results are shown for two Prandtl numbers: $Pr = 82.6$ (solid line) and $Pr = 7.0$ (dashed line). The vanishing of hysteresis marks a change in the nature of the hexagons, from the ℓ-type for smaller gain to the g-type for larger gain. For the RB limit in the range of $K_p = 0$ and 2.5, k_c increases from 2.09 to 3.35 whereas Ra_c increases from 669 to 1625.

Figure 6(*b*) (thin lines) shows the hysteresis in this limit for case (I) for the same values of Pr. The stable subcritical solution belongs to the g-type. As K_p increases, the magnitude of hysteresis increases slowly at first and then rapidly. The hysteresis diverges when $K_p \approx 2.55$ for both values of Pr. Although these values of K_p are near the onset of oscillatory instability, examining the coefficients q and g of (3.3) indicates that q continues to increase mildly in the diverged region, but the divergence in hysteresis is due to the vanishing of $g = (g_p + 2g_c)$, which changes sign at $K_p \approx 2.7$. When $g = 0$, higher-order nonlinear terms have to be considered in the amplitude expansion. The relatively strong hysteresis for the RB limit of figure 6(*b*) (thin lines) was not known prior to this study since a small-gain analysis was done by Shortis & Hall (1996), which is not valid for large $\hat{\epsilon}_N$. In contrast, the hysteresis for the BM limit is relatively mild.

We now consider case (I) for the two-layer setting, again based on the parameter values for the experiment of Schatz *et al.* (1995). The results are also shown in figure 6(*a*, *b*) (thick lines). A comparison between the cases of $Bi_{eff} = 0$ and the two-layer case suggests a very similar behaviour.

The results for case (II) provide a comparison concerning the sensitivity of the behaviour with respect to the method of thermal control. In figures 6(*c*)–6(*d*), using

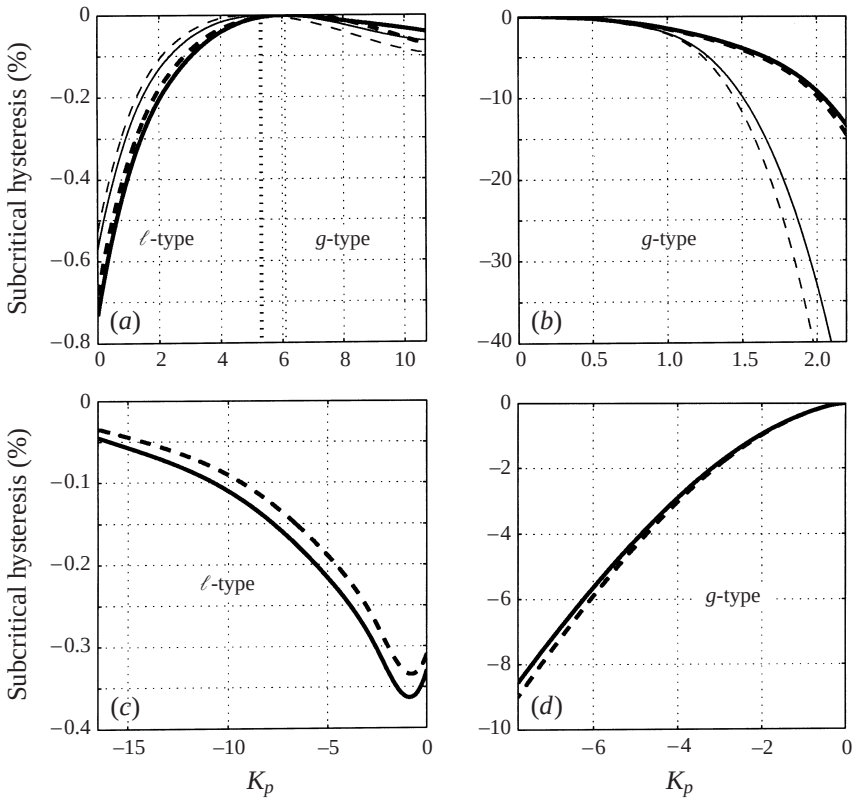

FIGURE 6. The subcritical hysteresis (in %) as a function of K_p for $Pr = 82.6$ (solid) and $Pr = 7$ (dashed). (*a*) Case (I) BM convection, $Bi_{eff} = 0$ (thin lines) and the two-layer model (thick lines); (*b*) case (I) RB convection, $Bi_{eff} = 0$ (thin lines) and the two-layer model (thick lines); (*c*) case (II) BM convection, the two-layer model only; (*d*) case (II) RB convection, the two-layer model only.

the parameters of the experiment in the two-layer model, we show the subcritical hysteresis for a comparison with figures 6(*a*)–6(*b*) (thick lines only) for the same values of Pr. For BM convection, there is no change in sign of the quadratic coefficient in the range of the monotonic solution of K_p. The subcritical hysteresis is significantly weaker for a given value of K_p. Furthermore, there is a dip near $K_p = -1$. For the RB limit, a trend similar to that of case (I) occurs. The subcritical hysteresis is still considered strong, but not as strong as in case (I). We conclude that the quantitative results are sensitive to the type of actuator used.

At this point, some qualitative understanding about the transition between the two hexagonal types is helpful. A schematic illustration of the physical mechanism is shown in figure 7 for the cases of weak and strong control. The symmetry-breaking term responsible for the preference of one type of cell over the other arises from the quadratic thermal advection at $O(\hat{\epsilon})$. From the basic equation (2.1*b*), the advection term $\boldsymbol{v}\cdot\nabla\theta$ can be expressed as $\nabla\cdot(\boldsymbol{v}\theta)$ since the flow is incompressible. On the upper and lower surface of a hexagonal cell, the term $\partial_r(v_r\theta)$ is responsible for the hexagon types. The preferred sense of motion is one that decelerates fluid moving from warm to cold regions. Consider the Pearson mode ($Ra = 0$) under a weak control. With weak control the maximum thermal contrast occurs near the upper surface. Since fluid decelerates on moving from warm to cold regions, it moves radially outward

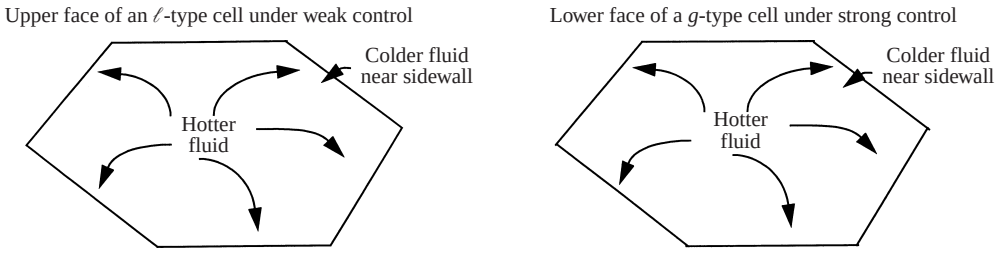

For weak control, fluid rises near centre and sinks near sidewalls. On the upper face, where a stronger thermal contrast occurs, the radially outward motion is consistent with the notion that fluid decelerates from hotter to colder regions.

For strong control, fluid sinks near centre and rises near sidewalls. On the bottom face, a stronger thermal contrast is imposed by the control temperature. Again, the radially outward motion is consistent with the notion that fluid decelerates from hotter to colder regions.

FIGURE 7. Schematic diagram for illustrating the physical mechanism responsible for the onset of ℓ- and g-types of hexagons.

giving rise to the ℓ-type hexagons. As the control action becomes stronger, it induces a stronger and stronger thermal contrast near the lower wall which is opposite to that near the upper surface. The sense of motion that occurs near the lower wall opposes the original preferred sense. Therefore, when the control is sufficiently strong, a reversal in sense of the motion occurs. In the reversed flow fluid moves radially outward rather than inward near the lower wall. The reversed flow is primarily driven by the control action and corresponds to the g-type hexagons.

So far, our results on feedback control are associated with a linear control law. In the linear feedback control of finite-amplitude disturbances, subcritical instability in general occurs. In controlling finite-amplitude disturbances, however, we can apply a quadratic gain tuned to eliminate the subcritical hysteresis. The idea was demonstrated to be effective for controlling secondary instability in a thermal convection loop, both theoretically and experimentally, by Yuen & Bau (1996). We have also discussed the method for controlling the onset of long-wavelength disturbances (Or *et al.* 1999). Figures 8(*a*)–8(*d*) show the quadratic gain K_q required to achieve such elimination as a function of K_p, namely $K_q = K_{q0} + K_{q1}/Pr$, at which the quadratic coefficient $q = q_0 + q_1/Pr = 0$. The three cases considered before, corresponding to figures 6(*a*)–6(*d*), are studied: (i) case (I) with $Bi_{eff} = 0$ for BM and RB convection (figure 8*a*, *b*, thin lines), (ii) case (I) with the experimental configuration of Schatz *et al.* (1995), for BM and RB convection (figure 8*a*, *b*, thick lines), and finally (iii) case (II) with the 1995 experiment configuration, for BM and RB convection (figure 8*c*, *d*). In general a cubic term is included in case a backwards pitch fork bifurcation occurs. But so far, such a situation has not occurred, unlike the long-wavelength case, and so the cubic control term has not been invoked. With K_q so chosen, supercritical bifurcation to rolls will occur.

In general the results of figures 8(*a*)–8(*d*) show that when K_p increases, the magnitude of K_q has to increase also. For RB convection, the relationship between the linear and quadratic gains is approximately linear. For BM convection, there is a quadratic dependence. In this case, the quadratic term in the amplitude equation is partly due to the control and partly due to the asymmetric mode of convection. But most importantly, the results indicate that a value of K_q can always be obtained to cancel the quadratic term that causes subcritical instability.

For the same control parameters, case (II) appears to be closer to the transition to a backward bifurcation than case (I). For instance, consider a moderate $K_p = 2.5$

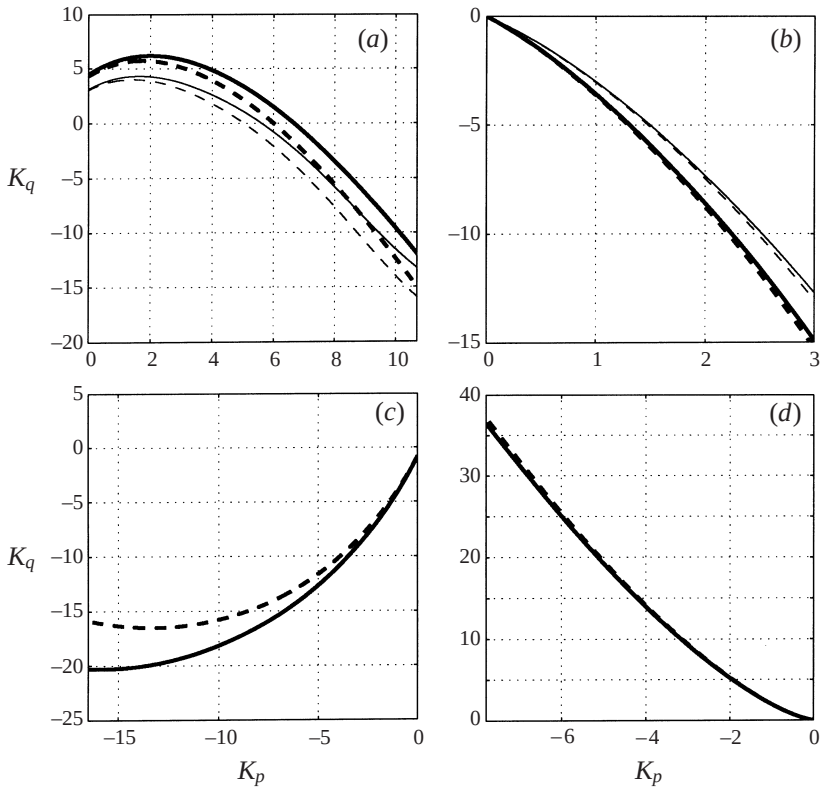

FIGURE 8. The quadratic gain $K_q = K_{q0} + K_{q1}/Pr$ required to eliminate the subcritical instability versus K_p. (*a*) Case (I) in the BM limit for $Bi_{eff} = 0$ (thin lines) and for the two-layer model (thick lines); (*b*) case (I) in the RB limit for $Bi_{eff} = 0$ (thin lines) and for the two-layer model (thick lines); (*c*) case (II) for the two-layer model in the BM limit only; (*d*) case (II) for the two-layer model in the BM limit only.

for case (I) and -2.5 for case (II). For the Marangoni limit, at large Pr it takes $K_c = -214$ for case (I) but only a value 18.5 for case (II) to revert the forward pitchfork bifurcation to a backward type. On the other hand, applying a K_c value in the direction of promoting the forward bifurcation has a suppressing effect on the amplitude of convection and therefore decreases the heat transport. For $K_c = 100$ (case (I)) coefficient g of (3.3) increases by 7.5% from its value at $K_c = 0$. For $K_c = -100$ (case (II)) g shows a significantly larger increase of 17%. Similar behaviour is observed for the RB limit.

4. Conclusions

We have studied Rayleigh–Bénard–Marangoni (RBM) convection using a two-layer model of a minimal type. The results are generally insensitive to the value of the thickness ratio d_g/d as long as $d_g/d > 0.5$. In the uncontrolled case, a comparison is made with the experimental results of Schatz *et al.* (1995). Significant discrepancy occurs in the value of Ma_c and also in the amount of subcritical hysteresis reported. On the other hand, our linear and weakly nonlinear results show reasonable agreement with other published theoretical results. Some possible reasons for the discrepancy were explored but found to be inadequate to explain it.

In the feedback control analysis, the stabilization of the basic state is limited by the onset of oscillatory instability in both RB and BM convection, in agreement with the predictions by Tang & Bau (1994), Bau (1999) and Howle (2000). For large Pr and appropriate Biot number the maximum ranges of stabilization (up to the onset of oscillatory mode) for both RB and BM limits are comparable. They are also comparable for both temperature and heat flux control, ranging approximately between 2 and 2.5 times the corresponding uncontrolled critical value.

The weakly nonlinear properties of convection, such as the type of hexagon and the amount of subcritical hysteresis, are significantly affected by feedback control. For purely BM convection, subcriticality is present when there is no feedback. The preferred hexagons switch from the ℓ-type to the g-type when K_p becomes sufficiently large for case (I). Subcritical hysteresis remains small even for large K_p. By contrast, for purely RB convection the bifurcation is supercritical when there is no feedback. In agreement with the prediction of Shortis & Hall (1996), the feedback control generates a subcritical instability and, as a result, g-type hexagons become preferred. But our results show further that a mild feedback tends to induce a relatively strong subcritical hysteresis. This result is not apparent in Shortis & Hall's analysis using a small-gain expansion approach. Because of the strong hysteresis the subcritical range as well as the stable range of hexagons tend to increase rapidly with K_p. The results for case (II) indicate a similar trend in the RB and BM limits, even though a switch of hexagon type has not been captured in the range and the amount of hysteresis is less.

A rather unexpected result is the divergent behaviour of subcritical hysteresis for the RB convection at moderately large gain. For case (I), the divergent behaviour occurs very close to the onset of oscillatory instability but for case (II), even though the hysteresis becomes large, divergence occurs outside the range of monotonic instability. However, there is no divergent behaviour for BM convection. The divergent behaviour is caused by the change in sign of the coefficient g in the amplitude equation, which suggests that higher-order nonlinear terms are necessary for the weakly nonlinear model or that a fully numerical analysis be done. Such an analysis would tell us whether control can be used effectively to augment heat transfer at subcritical values of Ra.

When hysteresis is present, large-amplitude disturbances will decay in general only when the operating value of Ma or Ra is below the turning point of the finite-amplitude subcritical branches. For strong subcritical hysteresis there can be a substantial difference between the maximum stable ranges of small- and large-amplitude disturbances. Like in the case of long-wavelength convection, here we have demonstrated that the subcritical range of convection can be removed by using a nonlinear feedback control law.

In order to complete the picture at the larger values of K_p, the analysis should be generalized to allow for the onset of oscillatory instability.

The authors would like to express their gratitude to M. Schatz, M. Bestehorn and G. Lebon for communications concerning the subcritical range in Marangoni–Bénard convection and to C. Pérez-García for kindly sending us a preprint of his paper with B. Echebarria and for his comments. This research was supported by the NASA Microgravity Fluid Physics Program (Grant no. NAG3-1819).

REFERENCES

Bau, H. H. 1999 Control of Marangoni–Bénard convection. *Intl J. Heat Mass Transfer* **42**, 1327–1341.

Bestehorn, M. 1993 Phase and amplitude instabilities for Bénard–Marangoni convection in fluid layers with large aspect ratio. *Phy. Rev.* E **48**, 3622.

Bestehorn, M. 1994 Pattern selection in Bénard–Marangoni convection. *Intl J. Bifurcation and Chaos* **4**, 1085–1094.

Bragard, J. & Velarde, M. G. 1998 Bénard–Marangoni convection: Planforms and related theoretical predictions. *J. Fluid Mech.* **368**, 165–194.

Clever, R. M. & Busse, F. H. 1993 Convection in a fluid layer with asymmetric boundary conditions. *Phys. Fluids* A **5**, 99–107.

Cloot, A. & Lebon, G. 1984 A nonlinear analysis of the Bénard–Marangoni problem. *J. Fluid Mech.* **145**, 447–469.

Echebarria, B. & Pérez–García, C. 2001 Stability of hexagonal patterns in Bénard–Marangoni convection. *Phys. Rev.* E (in press).

Golovin, A. A., Nepomnyashchy, A. A. & Pismen, L.M. 1995 Pattern formation in large-scale Marangoni convection with deformable interface. *Physica* D **81**, 117–147.

Howle, L. E. 1997*a* Linear stability analysis of controlled Rayleigh–Bénard convection using shadowgraphic measurement. *Phys. Fluids* **9**, 3111–3113.

Howle, L. E. 1997*b* Control of Rayleigh–Bénard convection in a small aspect ratio container. *Intl J. Heat Mass Transfer*, **40**, 817–822.

Howle, L. E. 1997*c* Active control of Rayleigh–Bénard convection. *Phy. Fluids* **9**, 1861–1863.

Howle, L. E. 2000 The effect of boundary properties on controlled Rayleigh–Bénard convection. *J. Fluid Mech.* **411**, 39–58.

Kang, Q. & Hu, W. R. 1999 Influence of the thickness ratio of air layer to liquid layer on the onset of Bénard–Marangoni convection. *Microgravity Sci. Techol.* **7**, 61–65.

Nield, D. A. 1964 Surface tension and buoyancy effects in cellular convection. *J. Fluid Mech.* **19**, 341–352.

Or, A. C., Kelly, R. E., Cortelezzi, L. & Speyer, J. L. 1999 Control of long-wavelength Marangoni–Bénard convection. *J. Fluid Mech.* **387**, 321–341.

Parmentier, P. M., Regnier, V. C., Lebon, G. & Legros, J. C. 1996 Nonlinear analysis of coupled gravity and capillary thermoconvection in thin fluid layer. *Phy. Rev.* E **54**, 411–423.

Pérez–García, C., Echebarria, B. & Bestehorn, M. 1998 Thermal properties in surface-tension-driven convection. *Phy. Rev.* E **57**, 475–481.

Regnier, V. C., Dauby, P. C. & Lebon, G. 2000 Linear and nonlinear Rayleigh–Bénard–Marangoni instability with surface deformations. *Phys. Fluids* **12**, 2797–2799.

Schatz, M. F., VanHook, S. J., McCormick, W. D., Swift, J. B. & Swinney, H. L. 1995 Onset of surface-tension-driven Bénard convection. *Phys. Rev. Lett.* **75**, 1938–1941.

Schatz, M. F., VanHook, S. J., McCormick, W. D., Swift, J. B. & Swinney, H. L. 1999 Time-independent square patterns in surface-tension-driven Bénard convection. *Phys. Fluids* **11**, 2577–2582.

Shortis, T. A. & Hall, P. 1996 On the effect of feedback control on Bénard convection in a Boussinesq fluid. *NASA Contractor Rep.* 198280; *ICASE Rep.* 96-9.

Smith, K. A. 1966 On convective instability induced by surface tension. *J. Fluid Mech.* **24**, 401–414.

Tang, J. & Bau, H.H. 1994 Stabilization of the no-motion state in the Rayleigh–Bénard problem. *Proc. R. Soc. Lond.* A **447**, 587–607.

Tang, J. & Bau, H. H. 1998*a* Experiments on the stabilization of the no-motion state of a fluid layer heated from below and cooled from above. *J. Fluid Mech.* **363**, 153–171.

Tang, J. & Bau, H. H. 1998*b* Numerical investigation of the stabilization of the no-motion state of a fluid layer heated from below and cooled from above. *Phys. Fluids* **10**, 1597–1610.

Thess, A. & Bestehorn, M. 1995 Planform selection in Bénard–Marangoni convection: ℓ-hexagons versus g-hexagons. *Phys. Rev.* E **52**, 6358–6367.

VanHook, S. J., Schatz, M. F., Swift, J. B., McCormick, W. D. & Swinney, H. L. 1997 Long-wavelength surface-tension-driven Bénard convection: experiment and theory. *J. Fluid Mech.* **345**, 45–78.

Wilcock, D. F. 1946 Vapor pressure-viscosity relations in Methylpolysiloxanes. *J. Am. Chem. Soc.* **68**, 691.

Yuen, P. K. & Bau, H. H. 1996 Rendering a subscritical Hopf bifurcation supercritical. *J. Fluid Mech.* **317**, 91–109.